Bayesian localization microscopy reveals nanoscale podosome dynamics

Susan Cox[1,7], Edward Rosten[2,3,7], James Monypenny[1], Tijana Jovanovic-Talisman[4], Dylan T Burnette[4], Jennifer Lippincott-Schwartz[4], Gareth E Jones[1] & Rainer Heintzmann[1,5,6]

We describe a localization microscopy analysis method that is able to extract results in live cells using standard fluorescent proteins and xenon arc lamp illumination. Our Bayesian analysis of the blinking and bleaching (3B analysis) method models the entire dataset simultaneously as being generated by a number of fluorophores that may or may not be emitting light at any given time. The resulting technique allows many overlapping fluorophores in each frame and unifies the analysis of the localization from blinking and bleaching events. By modeling the entire dataset, we were able to use each reappearance of a fluorophore to improve the localization accuracy. The high performance of this technique allowed us to reveal the nanoscale dynamics of podosome formation and dissociation throughout an entire cell with a resolution of 50 nm on a 4-s timescale.

High-resolution optical microscopy methods have pushed the resolution of a microscope system beyond the Abbe limit by using a nonlinear sample response to illumination light[1]. This result is often achieved by switching fluorophores between a dark and a bright state[2]. Stimulated emission depletion (STED) can be used to shrink the effective size of the scanning beam in a confocal system[3]; saturated structured illumination (SSIM) can extract information hidden in the *moiré* patterns produced when a grating is projected onto the sample[4]; and localization microscopy techniques, such as photoactivatable localization microscopy (PALM)[5] and stochastic optical reconstruction microscopy (STORM)[6], build a high-resolution image from the localized positions of many single fluorophores. The application of these techniques to live-cell imaging promises dynamic information on complex protein structures with nanoscale resolution[7–10]. The ideal microscopy technique would be experimentally simple and fast and would have the property that switching between fluorophore states would not damage the sample. However, several factors still limit the utility of high-resolution microscopy techniques for live-cell imaging applications.

STED requires a specialized microscope and a complex alignment procedure. On live cells, STED has achieved 28 frames per second at 62-nm resolution with low photon numbers over a field of view of 2.5 × 1.8 μm (ref. 9). As STED is a scanning technique, increasing the field of view decreases the frame rate. SSIM is not limited in this way because it is a wide-field technique; however, SSIM also requires a specialized microscope and can be prone to deconvolution artifacts[4], and biological high-resolution images obtained using SSIM have not yet been published. Non-saturated structured illumination (SIM) has been carried out at frame rates up to 11 Hz in live cells[11] but can provide around 100 nm resolution at most.

Current localization techniques require images in which the fluorescence emission from individual fluorophores does not overlap. This limits the number of fluorophores that can be localized in a given frame and thus the timescale at which useful images of complex structures can be acquired. Achieving the non-overlapping fluorophore emission necessary for conventional localization microscopy analysis requires switching a large fraction of probes into a non-emitting state. This is done either by activating small populations of fluorophores (usually using near-UV light) while imaging with longer wavelengths[5,6,12] or by keeping a large fraction of the probes in a non-emitting state using relatively high-intensity illumination (kW cm^{-2}) at a single imaging wavelength under suitable chemical conditions[13,14]. These wavelengths and intensities have been shown to damage live samples[15]. Current localization techniques have, however, allowed localization-based imaging of simple structures in live cells at a temporal resolution of 10 s without near-UV activation light[7] and at a temporal resolution of 0.5 s with near-UV activation light[10].

Another method that uses fluorescence blinking to boost the achievable resolution is called super-resolution optical fluctuation imaging (SOFI) and has been shown to improve images of samples labeled with quantum dots and organic dyes[16,17]. This method assumes that the blinking of neighboring fluorophores is uncorrelated and uses the temporal correlation between pixels of the image to sharpen the effective point-spread function. Analyzing 1,000-frame datasets of biological samples leads to a 1.4- to 2-fold improvement in resolution[17]. There are two other image analysis methods that are able to deal with relatively dense localization data: DAOSTORM[18] and simultaneous multiple emitter fitting[19]. These methods can analyze localization

[1]Randall Division, King's College London, Guy's Campus, London, UK. [2]Department of Engineering, University of Cambridge, Cambridge, UK. [3]Computer Vision Consulting Ltd., Lynton House, Woking, Surrey, UK. [4]National Institutes of Health, Cell Biology and Metabolism Branch, Bethesda, Maryland, USA. [5]Institute of Physical Chemistry, Friedrich-Schiller University Jena, Jena, Germany. [6]Institute of Photonic Technology, Jena, Germany. [7]These authors contributed equally to this work. Correspondence should be addressed to S.C. (susan.cox@kcl.ac.uk).

RECEIVED 25 DECEMBER 2010; ACCEPTED 2 NOVEMBER 2011; PUBLISHED ONLINE 4 DECEMBER 2011; DOI:10.1038/NMETH.1812

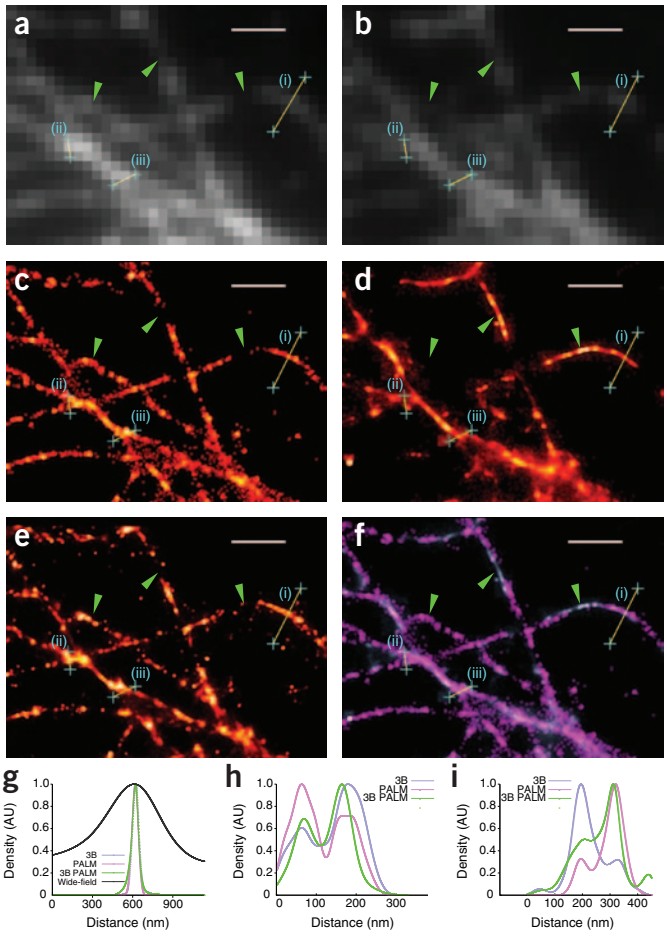

Figure 1 | Correlative measurements using PALM imaging and Bayesian localization imaging on tubulin. (**a**,**b**) Wide-field images created by averaging all the frames in the PALM image dataset of PA-GFP–tubulin (**a**) and by averaging all of the frames in the Bayesian localization image dataset of mCherry-tubulin (**b**). (**c**,**d**) Super-resolution images generated by analyzing the PALM PA-GFP–tubulin dataset from **a** using a standard PALM analysis[5] (**c**) and by analyzing the mCherry-tubulin dataset from **b** using a 3B analysis (**d**). (**e**) An image generated from the PAGFP dataset from **a** using a 3B analysis. (**f**) Overlay of **c** and **d**. Green arrows indicate regions with differences in apparent structure that arise from labeling differences. Linescans corresponding to lines i–iii are shown in **g**–**i**, respectively, with the 3B analysis data shown in blue, PALM data shown in pink, the 3B analysis PALM data shown in green and the wide-field data shown in black. Scale bars, 1 μm. AU, arbitrary units.

microscopy data that contain some overlapping fluorophores in each image, but they do not use the reappearance of fluorophores to improve localization.

Podosomes are cytoskeletal structures associated with cell adhesion, migration and degradation of the extracellular matrix[20,21]. They consist of an actin core surrounded by a ring of integrin-associated proteins such as talin and vinculin. This ring was thought to be roughly round, and the podosomes were thought to form and dissociate over a period of about 5–10 min. In wide-field images, the process of formation and dissociation appears as a fading out of the structure[22], although we have also seen instances where the podosome appears to slowly unwind.

Here we present a Bayesian localization microscopy method that allows localization data to be extracted from wide-field images of live cells labeled with a standard fluorescent protein. Our method allows the use of data from overlapping fluorophores as well as the use of information from bleaching events, blinking events and changes caused by fluorophores being added or removed in the cell. We carried out high-frame-rate imaging on a standard wide-field microscope with xenon arc lamp illumination. We used a Bayesian technique to model the resulting high-density fluorophore image data as arising from a number of fluorophores, each of which can emit light but which do not necessarily emit light in every frame. By modeling the whole dataset as arising from a number of fluorophores, we were able to use all of the fluorophore reappearances, even those in non-adjacent frames, and thus use all the photons collected from a fluorophore to improve our determination of its position. This 3B analysis method allowed us to perform localization microscopy with a spatial resolution of 50 nm and a temporal resolution of 4 s on podosomes in living cells expressing a monomeric (m)Cherry fusion of a truncated talin construct. Resolution here is defined as the smallest distance at which two talin strands can be separated, and the localization is defined as the apparent full width at half maximum (FWHM) of a strand of talin. We found that podosomes frequently have a polygonal structure and are highly dynamic over a timescale of tens of seconds.

RESULTS

Standard fluorescent proteins have been shown to blink and bleach in a live-cell environment, even under illumination from standard non-laser light sources. We developed the 3B analysis method to model an entire dataset consisting of a sequence of high-frame-rate images generated from large numbers of fluorescent proteins or other fluorophores undergoing blinking and bleaching processes. We modeled the entire dataset using a factorial hidden Markov model[23]. In this Bayesian technique, the state of a system at a certain time point is determined by both a transition matrix and the state of the system at the previous time point. The state of the system is statistically linked to the measured data (the link is not direct, as the measurement process itself is subject to noise). To render the calculation both accurate enough for optimization and algorithmically tractable, we hybridized two hidden Markov model inference methods: the forward algorithm[24] and Markov chain Monte Carlo sampling (MCMC) (Online Methods). We calculated many statistical samples of the model parameters, used these samples to generate fluorophore positions and built a probability map of the positions of the fluorophores taken from these samples. Each calculation of a particular set of model parameters used samples of the state taken using MCMC and generated a set of fluorophore positions using a maximum a posteriori (MAP) calculation.

If there were multiple models that fitted the data well, then it was very likely that we had samples of both models. At the end, we marginalized out the fluorophore state to give a distribution of fluorophore positions. Using this method, any ambiguity will cause the final model to be blurred out, making it unlikely that one would report falsely high resolution where there is actually ambiguity (where resolution is defined as the ability to image two fluorophores or line structures as separate). Although there exists only one model that corresponds to the real world, given the data, it is not possible to decide which one this model is, and averaging a multitude of models that are close to being correct seems to be an effective way of representing the underlying structure. A subtle yet key point is that this analysis is integrating over the parameters (both state sequences and

all continuous parameters; see **Supplementary Note**). The output is not a single model; rather, the output is an ensemble of models for different samplings of the state sequences. For each model in the ensemble, the optimized positions of the fluorophores are shown, but these positions are also integrated out when making the determinations of the number of fluorophores in the image. So the outcome of the analysis does not include a specific state sequence; the outcome has integrated over a sampling of different possible state sequences.

Correlative results

To verify that the 3B analysis produces a result that reflects the underlying structure when used on experimental (rather than simulated) data, we performed correlative experiments. We chose to label tubulin because the network of tubulin strands gives rise to strands crossing at many different distances and angles, which allows the resolution to be assessed by determining when the strands can be distinguished. We labeled tubulin with PA-GFP for PALM imaging and with mCherry for Bayesian localization imaging using a 3B analysis (**Fig. 1**). The wide-field images we created by averaging the frames in the two datasets (**Fig. 1a**,**b**) showed that not all features visible in one dataset are visible in another, as the incorporation efficiencies of mCherry and PA-GFP into the microtubule vary. The incorporation of these proteins into the microtubule was low, so some areas had more mCherry-tubulin and other areas had more PA-GFP–tubulin. Some areas that showed a particularly clear discrepancy between the labeled areas even in the wide-field microscopy images are indicated with green arrows (**Fig. 1a**–**f**).

Using a 3B analysis, we created a probability map by building up many MAP positions obtained from different samplings of state sequences (**Fig. 1d**). As a result of the high amount of fluorophore overlap in all the frames, this mCherry data was not analyzable using standard localization microscopy analysis techniques. With the exception of the labeling discrepancies noted above, the 3B analysis results (**Fig. 1d**) were in good agreement with the PALM data (**Fig. 1c**),with features separated by distances as small as 100 nm being visible in both datasets; and when features were present in both datasets, they agreed to a high resolution, as shown in the overlay of the PALM and 3B analysis images (**Fig. 1f**). Additionally, applying the 3B analysis to the PALM dataset yielded a very similar structure as the original PALM analysis (**Fig. 1e**).

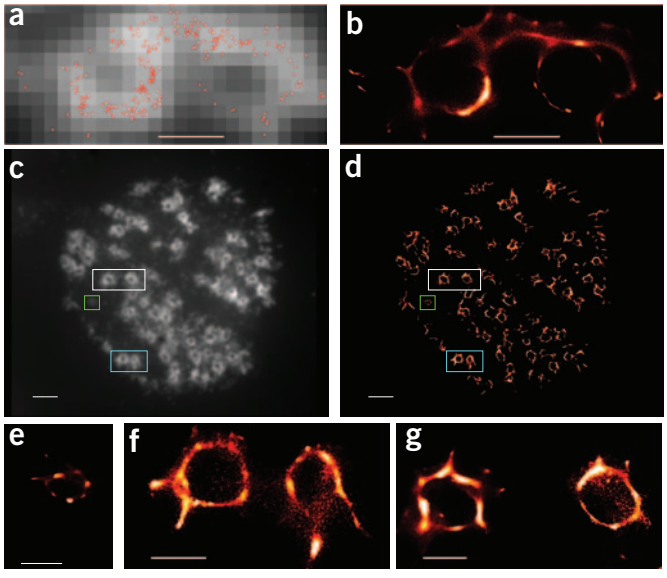

Figure 2 | A 3B analysis of vinculin in fixed cells containing podosomes and labeled with Alexa 488. (**a**) An example of a maximum likelihood estimate for one set of MCMC samples superimposed on a wide-field image created by averaging all 300 images. (**b**) A probability map created by combining MAP positions created using different sets of MCMC samples. Scale bars, 500 nm. (**c**,**d**) A whole cell showing a wide-field (**c**) and 3B analysis (**d**). The green rectangle corresponds to the enlarged image in **e**, the blue rectangle corresponds to the enlarged image in **f**, and the white rectangle corresponds to the enlarged image in **g**. Scale bars, 500 nm (**a**,**b**); 2 mm (**c**,**d**); and 500 nm (**e**–**g**).

Experiments on fixed podosomes

We immunolabeled vinculin in fixed podosome samples with Alexa 488 and mounted the samples in PBS (pH 7.25) with 100 mM 2-mercaptoethanol that we added as a reducing agent to induce blinking[14] (**Supplementary Fig. 1**). We illuminated the sample using a laser at 488 nm with a nominal power of 1kW cm^{-2}. We collected a series of 300 images, with collection taking a total of 6 s. A video of the raw data is shown as **Supplementary Video 1**. It is notable that there were many overlapping emitting fluorophores in the majority of the frames. This prevented us from using the standard thresholding and fitting-image analysis techniques normally used to reconstruct PALM or STORM images. A typical wide-field image obtained by averaging all 300 images is shown as the background in **Figure 2a**. An example of the MAP positions created from one sampling of the 3B analysis is shown in red in **Figure 2a** (many MAP positions were combined to create the final probability map, shown in **Fig. 2b**).

The apparent thickness of the vinculin strands varied between 6 nm and 60 nm, with the variation probably arising from variation in the number of fluorophore reappearances in different areas, the number of photons detected in one appearance and variations in the distribution of vinculin. The structure of the podosome was geometrical, which is in agreement with recent high-resolution microscopy observations obtained using STED and SIM (at a resolution of approximately 120 nm) (M. Walde, J.M., G.E.J., R.H., S.C., unpublished data). The higher resolution revealed a small structure joining the two podosomes.

We applied the 3B analysis to an entire cell (**Fig. 2c**–**g**). This application revealed a small number of podosomes with a diameter of less than 300 nm, well below the standard diameter of around 500 nm (**Fig. 2e**), which only appeared as a blob of brightness in the wide-field image. As in SIM and STED studies of podosomes (M. Walde, J.M., G.E.J., R.H., S.C., unpublished data), vinculin strands tended to bind at angles of 120–130° (**Supplementary Fig. 2**).

Experiments on podosomes in living cells

We generated cells from the human acute monocytic leukemia cell line THP1 that stably expressed an mCherry-tagged, truncated talin construct (amino acids 1,974–2,541) using lentiviral gene transduction. The resulting talin mutant comprised the second integrin binding domain of talin and has previously been shown to be an excellent marker of podosome rings in living cells[25]. We illuminated live samples (maintained at 37 °C) with a mercury arc lamp supplying a nominal power (measured before the objective) of 12 W cm^{-2} to the sample in the wavelength range of 615–687 nm and acquired a series of 5,000 images at 50 frames per second. An example of the data obtained from this experiment is shown as **Supplementary**

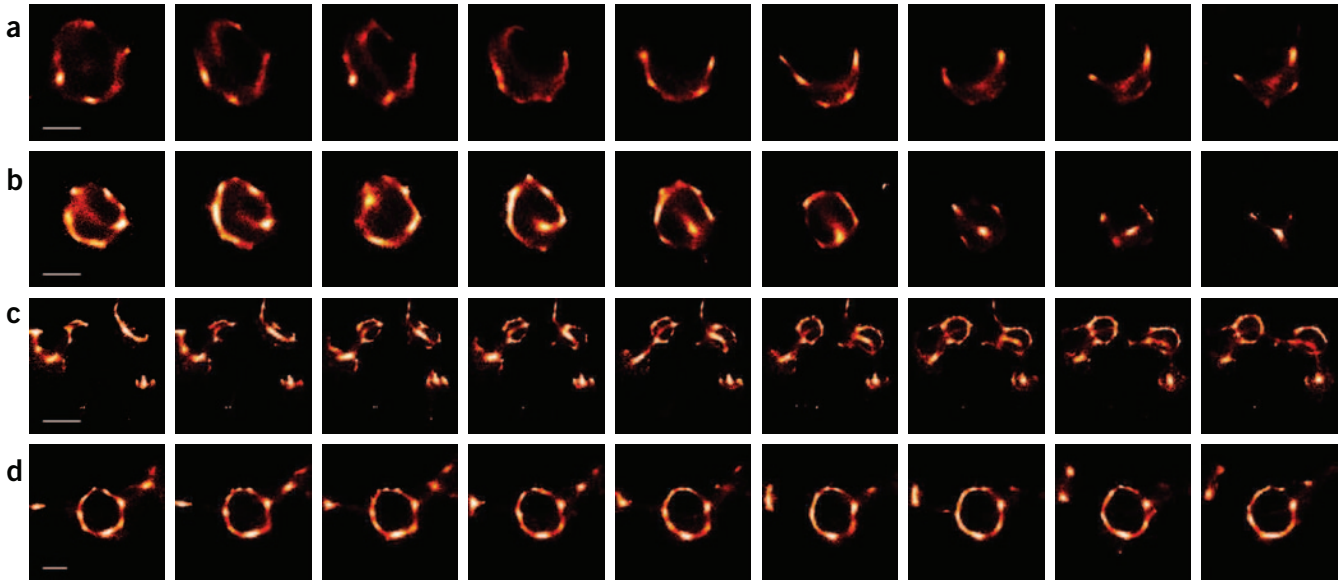

Figure 3 | Podosomes, visualized using an mCherry-tagged truncated talin construct, forming and dissociating in a live cell. (**a**,**b**) A podosome being dissociated. Scale bars, 400 nm. (**c**) Podosomes being formed. Scale bar, 1 μm. (**d**) A steady-state podosome. Scale bar, 400 nm. Each reconstructed frame used 200 frames (4 s), and frames are spaced 600 frames (12 s) apart. Videos of the podosomes shown in **a**–**d** are provided as **Supplementary Videos 3**–**6**, respectively.

Video 2. We applied the 3B analysis to sequences of 200 frames, which corresponds to an acquisition time of 4 s. In **Figure 3**, data are shown for selected time points from the reconstructed image sequence. The complete reconstructed datasets are shown in **Supplementary Videos 3**–**6**, with the timeshift between video frames being either 50 frames or 0.5 s (though the temporal resolution is still 4 s in these videos).

We determined the localization precision from the FWHM of a linescan that was perpendicular to a talin strand to be as good as 18 nm. We defined the resolution as the distance at which two talin strands could be visually separated, as measured by a linescan. We determined the resolution here to be 50 nm (**Supplementary Fig. 3**).

Movement of the fluorophores will cause an analysis to produce an image that is smeared in the direction of the movement. This effect limits the resolution that is achievable if structures are moving by distances larger than the resolution of the system on timescales smaller than the acquisition time for a single reconstructed high-resolution image. We chose podosomes as a suitable test system for our imaging analyses, as they form and dissociate over a period of several minutes, and most podosomes do not appear to move around the cell during this time (if podosome movement is observed, it is generally restricted to a few hundred nm).

We observed podosomes undergoing assembly and two different modes of breakdown. In the first mode of podosome breakdown, the podosome shows a small break, and then one end of the break gradually retracts, producing an 'unwinding' effect (**Fig. 3a**). This retraction seems to be associated with the formation of small (250 nm in diameter) struts in the region of the cell where the podosome is being dissociated. In the second mode of podosome dissociation, struts (approximately 450 nm in length) repeatedly form

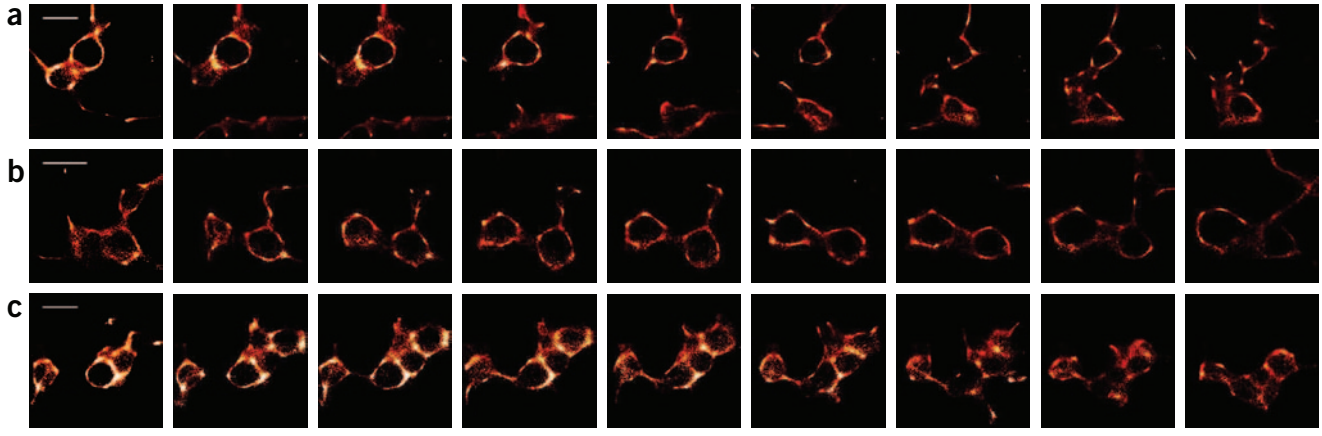

Figure 4 | Dissociation and formation of groups of podosomes in a motile cell. (**a**,**b**) Dissociation and formation of linked podosomes. (**c**) Separated podosomes joining together. Each reconstructed frame used 200 frames (4 s), and frames are spaced 1,000 frames (20 s) apart. A video containing the podosomes shown in **a**–**c** as well as the rest of the cell is provided as **Supplementary Video 7**. Scale bars, 800 nm.

across the podosome, drawing the talin in to a central point until it has been removed (**Fig. 3b**). We also observed podosome formation in which the strut seemed to have a crucial function, with the podosome nucleating from a strut and then expanding on either side of it (**Fig. 3c**). Once the podosome had formed and the strut had served its purpose, it appeared to be broken down. Some podosomes showed no apparent changes in the wide-field image and were relatively stable at the nanoscale (**Fig. 3d**).

We also observed more complex structures composed of a number of joined podosomes and struts. Imaging of a motile cell revealed highly dynamic behavior of these complex structures, with podosome structures changing on a timescale of tens of seconds. **Figure 4** depicts one example of such behavior, where two groups of podosomes become joined after each group extends a strut. Where the two struts join, a miniature podosome-like structure forms, and the two groups of podosomes are pulled closer together. We saw similar behavior across the whole cell (**Supplementary Video 7**).

To determine whether the truncated talin construct that we used for our live-cell imaging experiments is representative of the structure of the podosome protein ring, we performed two-color measurements in fixed cells. We fixed cells expressing the mCherry-tagged truncated talin construct, and we immunolabeled vinculin with Alexa 488–tagged secondary antibody. We used the same embedding conditions that we used for the other fixed-cell experiments. The truncated talin construct and the vinculin had similar distributions (**Fig. 5**). The vinculin image was localized slightly more to the periphery of the ring, and the talin was more localized to the center, whereas the short strands at the edge of the ring were more visible in the vinculin. This hints that the localization of different proteins in the ring are subtly different and shows that the 3B analysis method can be used to build a map of the spatial organization of different podosome components.

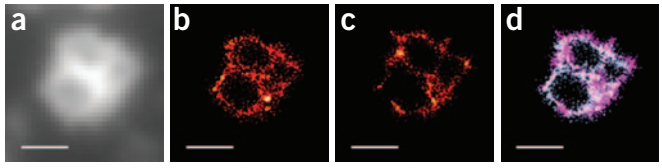

Figure 5 | A 3B analysis of fixed-cell data to determine the colocalization of vinculin and the truncated talin construct in podosomes. (**a**) Wide-field image of vinculin labeled with Alexa 488. (**b**,**c**) The individual 3B analysis images shown in glowscale for talin (**b**) and vinculin (**c**). (**d**) Superposition of images from the 3B analysis showing the truncated talin construct (in cyan) and vinculin 3B data (in magenta). Scale bars, 1 μm.

Simulations

To further validate the Bayesian localization imaging results from our 3B analysis method, we analyzed simulated datasets. Bayesian fitting methods use wide priors over a large number of parameters to fit real-world data, which tend to have narrow, unknown distributions over these parameters. Simulations created using the fitting distributions may not provide good results, so we created simulated datasets by using blinking sequences and fluorophore positions from the PALM correlative data. We created each simulated frame using the fluorophore positions from 16 PALM frames (**Fig. 6**). The average separation of two nearest-neighbor fluorophores was 112 nm, which is considerably smaller than the point spread function FWHM (270 nm), leading to a large amount of fluorophore overlap in simulated the frames (**Fig. 6g**,**h**).

The simulations showed that the 3B analysis method achieves 50-nm resolution at an intersection of two strands (**Figs. 6i**,**j**). This method produced the correct structure but did not pick up every fluorophore. We observed artificial thinning and thickening of the structures in different areas, but the magnitude of all of these effects was less than 20 nm. In all instances, the intensity between close spots was somewhat enhanced, making the spots appear more 'connected' than they were in the PALM data. This enhanced intensity suppressed the resolution along a line of fluorophores compared to the resolution perpendicular to a line of fluorophores. We quantified the resolution perpendicular to lines of fluorophores in all our experiments.

DISCUSSION

The 3B analysis method removes a number of barriers to getting the good localization information that can be obtained using other approaches. The experiments for 3B analysis are easy to implement: live cell experiments use fluorescent proteins, a wide-field microscope and arc lamp illumination, which are all standard in most cell biology labs. With this equipment, it is possible to achieve a 50-nm resolution with data from only a few seconds of acquisition, and it is possible to image for extended time periods. The software that we used to perform the analysis here is provided in the **Supplementary**

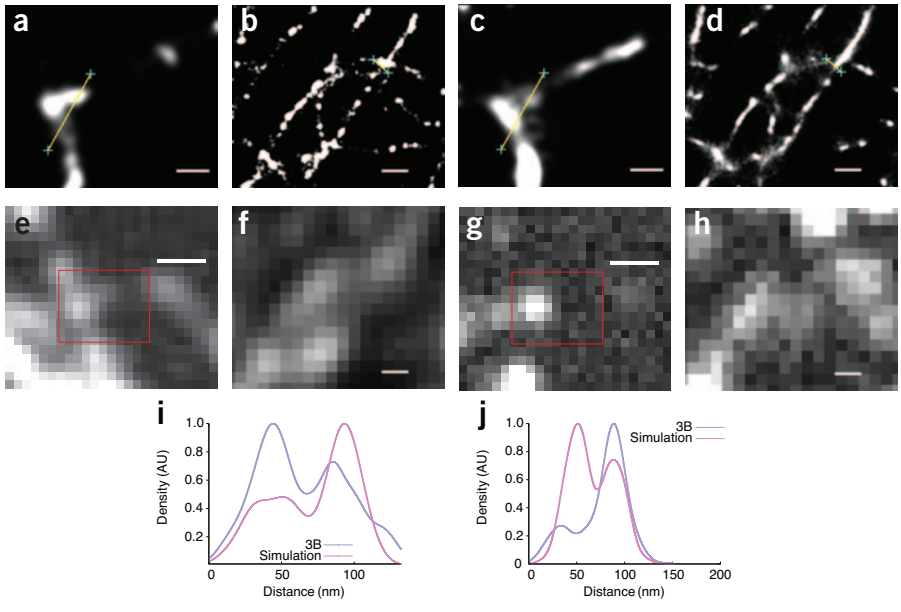

Figure 6 | Simulations showing the performance of the 3B analysis method. (**a**–**d**) Ground truth simulated image data (**a**,**b**) and 3B analysis reconstructions (**c**,**d**). (**e**–**h**) For the simulations, the simulated wide-field image created by averaging all frames (**e**,**f**) and a typical frame (**g**,**h**) are shown. Images in **a** and **c** correspond to the boxed regions in **e** and **g**, respectively. (**i**,**j**) Linescans of the simulations and 3B analysis reconstructions show the 3B analysis method achieving good reproduction of the structure and a resolution of 50 nm. Scale bars, 50 nm (**a**,**c**); otherwise, 200 nm.

Software; updated versions of the software can be obtained from http://3bmicroscopy.com.

The computational effort of our method is linear with respect to the number of fluorophores multiplied by the number of pixels. For a cell such as that shown in **Figure 2**, we modeled the data as arising from 10,000 fluorophores, and we used 200 sets of MCMC samples to build the probability map.

To analyze a region of around 1.5 × 1.5 μm in size, processing on a single core i7 (3.33 GHz) for 6 h is required. Larger areas can be analyzed, but the time required for these analyses scales with the area of the region. To analyze large areas, the analysis is broken down into a number of small areas. To analyze large images or video data, a cluster computer is required.

Our method has a natural mechanism for trading off temporal and spatial resolution: analyzing more frames simultaneously raises the spatial resolution but lowers the temporal resolution. Comparing our method to SOFI, both methods can deal with images that have overlapping fluorophores, but SOFI requires more data and delivers a more limited resolution improvement than the 3B analysis. In the 3B analysis, it is possible to artificially sharpen structures by including models with fewer fluorophores than the data, but in simulations, we found these effects to be considerably below the resolution limit.

Rather than revealing an improved resolution picture of an apparently smooth process in podosomes, achieving high resolution revealed an entirely new level of complexity. Podosomes were previously thought to smoothly form and dissociate over a period of several minutes[22]. However, our results indicate that podosomes are highly dynamic structures. It appears that smaller ring-type structures down to 230 nm play a crucial part in podosome dynamics. Rather than strands simply being parts of partially grown podosomes, our results indicate that these structures may have a role in seeding new areas of podosomes. In another form, as struts spanning across a podosome, they appear to be associated with podosome formation and dissociation.

Our use of standard fluorescent proteins opens the techniques of high spatial and temporal resolution microscopy to a whole new range of samples. Many of these samples, like podosomes, may be complex all the way down to the nanoscale.

METHODS

Methods and any associated references are available in the online version of the paper at http://www.nature.com/naturemethods/.

Note: Supplementary information is available on the Nature Methods website.

ACKNOWLEDGMENTS

We acknowledge helpful discussions with A. Fraser, F. Viola, P. Fox-Roberts, O. Mandula and J. Sleep. We thank M. Kielhorn for assistance in aligning the optical system and K. Glocer for critical reading of the manuscript. We thank M. Parsons (King's College London) for providing the template plasmid. We acknowledge support from the EU Seventh Framework Programme (FP7 Project GA 215597 (S.C. and R.H.), EU FP7 Project ITN 237946 T3Net (G.E.J.)), the Wellcome Trust (S.C., J.M. and G.E.J.), the Medical Research Council (UK) (G.E.J.) and the Royal Society (S.C.).

AUTHOR CONTRIBUTIONS

S.C., J.M., T.J.–T., D.T.B., J.L.-S., G.E.J. and R.H. conceived of and designed the experiments. S.C. and E.R. conceived of and designed the analysis. J.M. prepared the podosome samples, and T.J.–T. and D.T.B. prepared the samples for correlative measurements. S.C. and J.M. performed live-cell experiments, S.C. carried out fixed-cell experiments on podosomes, and T.J.–T. and D.T.B. carried out the correlative measurements. E.R. and S.C. carried out the data analysis and wrote the manuscript, and all authors revised the manuscript.

COMPETING FINANCIAL INTERESTS

The authors declare no competing financial interests.

Published online at http://www.nature.com/naturemethods/.
Reprints and permissions information is available online at http://www.nature.com/reprints/index.html.

1. Heintzmann, R. & Ficz, G. Breaking the resolution limit in light microscopy. *Methods Cell Biol.* **81**, 561–580 (2007).
2. Hell, S.W. Microscopy and its focal switch. *Nat. Methods* **6**, 24–32 (2009).
3. Klar, T.A., Jakobs, S., Dyba, M., Egner, A. & Hell, S.W. Fluorescence microscopy with diffraction resolution barrier broken by stimulated emission. *Proc. Natl. Acad. Sci. USA* **97**, 8206–8210 (2000).
4. Heintzmann, R., Jovin, T.M. & Cremer, C. Saturated patterned excitation microscopy—a concept for optical resolution improvement. *J. Opt. Soc. Am. A* **19**, 1599–1609 (2002).
5. Betzig, E. *et al.* Imaging intracellular fluorescent proteins at nanometer resolution. *Science* **313**, 1642–1645 (2006).
6. Rust, M.J., Bates, M. & Zhuang, X. Sub-diffraction-limit imaging by stochastic optical reconstruction microscopy (STORM). *Nat. Methods* **3**, 793–796 (2006).
7. Wombacher, R. *et al.* Live-cell super-resolution imaging with trimethoprim conjugates. *Nat. Methods* **7**, 717–719 (2010).
8. Shroff, H., Galbraith, C.G., Galbraith, J.A. & Betzig, E. Live-cell photoactivated localization microscopy of nanoscale adhesion dynamics. *Nat. Methods* **5**, 417–423 (2008).
9. Westphal, V. *et al.* Video-rate far-field optical nanoscopy dissects synaptic vesicle movement. *Science* **320**, 246–249 (2008).
10. Jones, S.A., Shim, S.-H., He, J. & Zhuang, X. Fast, three-dimensional super-resolution imaging of live cells. *Nat. Methods* **8**, 499–505 (2011).
11. Kner, P., Chhun, B.B., Griffis, E.R., Winoto, L. & Gustafsson, M.G.L. Super-resolution video microscopy of live cells by structured illumination. *Nat. Methods* **6**, 339–342 (2009).
12. Heilemann, M., Dedecker, P., Hofkens, J. & Sauer, M. Photoswitches: key molecules for subdiffraction-resolution fluorescence imaging and molecular quantification. *Laser Photonics Rev.* **3**, 180–202 (2009).
13. Zhuang, X. Nano-imaging with STORM. *Nat. Photonics* **3**, 365–367 (2009).
14. Heilemann, M., van de Linde, S., Mukherjee, A. & Sauer, M. Super-resolution imaging with small organic fluorophores. *Angew. Chem. Int. Ed.* **48**, 6903–6908 (2009).
15. Lippincott-Schwartz, J. & Manley, S. Putting super-resolution fluorescence microscopy to work. *Nat. Methods* **6**, 21–23 (2009).
16. Dertinger, T., Colyera, R., Iyera, G., Weissa, S. & Enderleind, J. Fast, background-free, 3D super-resolution optical fluctuation imaging (SOFI). *Proc. Natl. Acad. Sci. USA* **106**, 22287–22292 (2009).
17. Dertinger, T., Heilemann, M., Vogel, R., Sauer, M. & Weiss, S. Superresolution optical fluctuation imaging with organic dyes. *Angew. Chem.* **122**, 9631–9633 (2010).
18. Holden, S., Uphoff, S. & Kapanidis, A. DaoSTORM: an algorithm for high-density super-resolution microscopy. *Nat. Methods* **8**, 279–280 (2011).
19. Huang, F., Schwartz, S.L., Byars, J.M. & Lidke, K.A. Simultaneous multiple-emitter fitting for single molecule super-resolution imaging. *Biomedical Optics Express* **2**, 1377–1393 (2011).
20. Linder, S. & Aepfelbacher, M. Podosomes: adhesion hot-spots of invasive cells. *Trends Cell Biol.* **13**, 376–385 (2003).
21. Linder, S. & Kopp, P. Podosomes at a glance. *J. Cell Sci.* **118**, 2079–2082 (2005).
22. Monypenny, J. *et al.* Role of WASP in cell polarity and podosome dynamics of myeloid cells. *Eur. J. Cell Biol.* **90**, 198–204 (2011).
23. Ghahramani, Z. & Jordan, M.I. Factorial hidden Markov models. *Mach. Learn.* **29**, 245–273 (1997).
24. Rabiner, L.R. A tutorial on hidden Markov models and selected applications in speech recognition. *Proc. IEEE* **77**, 257–286 (1989).
25. Wiesner, C., Faix, J., Himmel, M., Bentzien, F. & Linder, S. KIF5B and KIF3A/KIF3B kinesins drive MT1-MMP surface exposure, CD44 shedding, and extracellular matrix degradation in primary macrophages. *Blood* **116**, 1559–1569 (2010).

ONLINE METHODS

Sample preparation for correlative measurements. B16-F1 cells were seeded on coverslips coated with 25 μg ml^{-1} laminin as previously described[26]. Cells were then co-transfected with PA-GFP–tubulin and mCherry-tubulin with FuGENE 6 (Roche) following the manufacturer's recommendations. Cells were fixed with 4% paraformaldehyde, 0.2% glutaraldehyde (Electron Microscopy Sciences) in PBS (pH 7.4) for 35 min at room temperature (18–25 °C). Streaming time-lapse images were acquired with an Olympus IX71 total internal reflection fluorescence microscope using a 60×, 1.45-numerical-aperture (NA) objective (Olympus), and fluorescence emission was detected with an electron-multiplying charge-coupled device (EM-CCD) camera (Andor Technology, DV887ECS-BV). PA-GFP constructs were imaged with 100 ms integration times (488-nm laser power was 400–800 μW going into the microscope). mCherry constructs were imaged with 50-ms integration times (561 nm laser power was 1 mW going into the microscope). PALM datasets comprised 5,000 frames, 3B datasets comprised 1,000 frames, and both datasets were corrected for drift. For the PALM data, single molecules were fitted with theoretical Gaussians, and PALM images were reconstructed as previously described[5].

Sample preparation for podosome observations. The THP1 cell line, which can be stimulated to differentiate into macrophages, was used to observe podosomes. Podosome formation was induced in these cells by seeding them on fibronectin-coated cover glasses in the presence of the cytokine TGF-β1 (1 ng ml^{-1}). Vinculin staining was conducted using VN-1 vinculin mouse monoclonal antibody (Sigma) conjugated to Alexa 488 mouse secondary antibody. Coverslips were mounted in PBS (pH 7.4) containing 100 mM 2-mercaptoethanol to induce blinking at a suitable rate[14].

Lentiviral-mediated gene transduction of THP1 cells. PCR was used to amplify cDNA encoding residues 1,975–2,541 of human talin from a template plasmid. The resulting sequence was cloned using the Zero Blunt vector (Invitrogen) into the multiple cloning site of the pLNT/Sffv-mCherry-MCS vector generating the mCherry-talin (1,975–2,541) lentiviral expression construct. VSV-G pseudotyped lentivirus encoding mCherry-talin (1,975–2,541) was packaged in 293T cells by transient transfection of the cells with the pΔ8.91 and pMD.G accessory plasmids along with the pLNT/Sffv transfer vector encoding the talin construct. Supernatants containing lentivirus were harvested 48 h after transfection, filtered through a 0.45-μm-pore-size filter and stored at –80 °C. THP1 cells were transduced with lentivirus by incubation with lentiviral supernatants for 24 h, then washed using sequential centrifugation and resuspension steps and left for an additional 3 d to express the fusion protein. Twenty-four hours before the live-cell imaging experiments, THP1 cells were seeded at a density of 2.5 × 10^6 cells per ml on fibronectin-coated (10 μg ml^{-1}) glass coverslips in the presence of 1 ng ml^{-1} TGF-β to induce cell attachment and podosome formation. For all imaging experiments, coverslips with adherent cells were mounted onto purpose-built glass viewing chambers. For the two-color experiments, cells containing the truncated mCherry-talin construct were fixed and stained as described previously.

Microscopy for the podosome experiments. For the fixed-cell experiments, a wide-field Zeiss Axiovert 200M microscope was used with an oil immersion objective (63×, NA 1.4; Zeiss) and a 2.5× Optovar. Illumination was provided by an argon ion laser (Innova 90 coherent) emitting at 488 nm. Images were recorded using a Cascade II EM-CCD camera (Photometrics) with square pixels and a pixel pitch of 16 μm (each recorded pixel corresponds to 102 nm in real space). The frame rate varied between 50 and 60 frames per second.

For the live-cell experiments, a wide-field Olympus IX81 was used with an oil immersion objective (100×, NA 1.4; Olympus). Illumination was provided by a Sutter Lambda LS xenon arc lamp coupled with a liquid light guide, with a Comar GFP-RFP filter set (for RFP, excitation was at 537.5–592.5 nm, emission was at 615–687 nm and dichroic was at 590–700 nm). Images were recorded using a Cascade II EM-CCD camera (with the same properties as the camera described above). For **Figure 3**, no post magnification was used, meaning each recorded pixel corresponded to 160 nm in real space. For **Figure 4**, a 1.6× post magnification was used, meaning that each recorded pixel corresponded to 100 nm on the sample. The drift in these experiments was assessed by monitoring the drift of the bead samples over time. The beads were imaged using the same frame rate and for the same amount of time as in the live-cell experiment. The drift was found to be within the localization error, with the mean of the localization position varying by up to 10 nm over 5,000 images (acquired over 98 s). We therefore ignored drift effects in our analysis, as the expected drift over the 200 images that we used to reconstruct an image was expected to be 0.4 nm.

Simulations. Simulations were created using fluorophore positions from 4,800 out of the 5,000 PALM frames, with each simulated frame created from 16 PALM frames, resulting in 300 simulated frames. The simulated frames were created from two groups of PALM frames such that simulated frame 0 consisted of PALM frames 0–7 and 2,400–2,407, simulated frame 1 consisted of PALM frames 8–15 and 2,408–2,415 and so on. This method prevented later frames from becoming unrealistically sparse. The FWHM of the simulated point spread function was set to 1.56 pixels, which corresponds to a FWHM of 270 nm at 86 nm per pixel (this halved the number of nm per pixel compared to the original PALM dataset, but because the positions of the fluorophores were set relative to pixels, it also decreased the distance between fluorophores by a factor of 2). This created datasets with overlapping fluorophores. Simulated images were created using Gaussian-shaped spots of average brightness 1,200 photons on a background of average brightness 600 photons with Poisson noise. The photon counts and, therefore, the signal-to-noise ratio was set using photon counts from the background and isolated fluorophores in the fixed-cell dataset.

Analysis. The image series was modeled using a factorial hidden Markov model[23] as arising from a number of fluorophores. Each fluorophore was modeled using a Markov model that had three possible states: emitting (light), non-emitting and bleached. The fluorophore can transfer between the emitting and non-emitting states and can also transfer from the non-emitting to the bleached state. Once in the bleached state, the fluorophore cannot leave it. The state transition diagram for fluorophores is shown in **Supplementary Figure 4**. From our estimates of the lifetimes and transition probabilities associated with the energy levels[14,27] and the frame time of around 0.02 s, we calculated estimates for all the model probabilities in a given frame. We obtained values of $P_1 = 0.16$, $P_2 = 0.84$, $P_3 = P_4 = 0.495$ and $P_5 = 0.01$ (see **Supplementary Fig. 4** and **Supplementary Note**

for definitions and discussion of these probabilities). To calculate these values, the typical values of the lifetimes and various transition probabilities were taken. The on-state lifetime was taken to be 10^{-7} s, and a fluorophore was taken to be 10^5 times more likely to remain in the on state than to transition to the off state. The frame rate of the camera was taken to be between 50 and 60 Hz (each frame takes 18 ms). So each frame is 18,000 on-state lifetimes, in each of which the fluorophore had a probability of 0.99999 of returning to the on state. The values of P_3 and P_4 were taken with a variety of typical off-state lifetimes (10^{-3}–10^{-2} s) assuming a monoexponential decay. This led to values of P_4 between 0.1 and 0.8. The value of 0.495 was chosen as being reasonably central to this spread, given the large uncertainties in the input values.

The same state transition probabilities were used for fitting both fixed-cell and live-cell datasets, as only a broadly correct prior is needed for this type of modeling. The structure observed in the reconstructed image did not vary to an extent that it altered the observed structure if the state transition probabilities were varied within physically realistic values. We assume that neighboring fluorophore states are statistically completely independent. Our results are only weakly dependent on the priors. Without blinking or bleaching, this method would have the same limits as deconvolution. To enhance the blinking, a switching probe with better dynamics could be used.

We calculated the relative probability that a fluorophore was present compared to the null hypothesis that the data arose from noise. The model evidence for each hypothesis can be calculated by integrating out over state sequences (the blinking and bleaching state in each frame) using the forward algorithm[24] and by integrating out over continuous variables using Laplace's approximation[28]. However, the forward algorithm calculation is exponential in the number of fluorophores. An alternative approach is to take a statistical sample of state sequences, but this method does not provide sufficiently accurate results. We therefore used a hybrid of the forward algorithm and a state-sampling technique. A detailed description of the algorithm is given in the **Supplementary Note**.

The algorithm is then run on user-selected areas. The user must specify the pixel size (which is used to calculate the predicted point spread function size) and the starting number of fluorophores in the area. The final result of the algorithm is a density map of the positions of fluorophores yielded. Further details on the parameters and reconstruction algorithm are given in the **Supplementary Note**.

26. Burnette, D.T. *et al.* A role for actin arcs in the leading-edge advance of migrating cells. *Nat. Cell Biol.* **13**, 371–382 (2011).
27. Xie, X.S. Optical studies of single molecules at room temperature. *Annu. Rev. Phys. Chem.* **49**, 441–480 (1998).
28. MacKay, D.J.C. *Information Theory, Inference, and Learning Algorithms* (Cambridge Univ. Press, 2003).

doi.10.1038/nmeth.1812

Nature Methods

Bayesian localization microscopy reveals nanoscale podosome dynamics

Susan Cox, Edward Rosten, James Monypenny, Tijana Jovanovic-Talisman, Dylan T Burnette, Jennifer Lippincott-Schwartz, Gareth E Jones & Rainer Heintzmann

Supplementary File	Title
Supplementary Figure 1	Blinking of fluorophores in fixed podosome sample
Supplementary Figure 2	Vinculin filament binding angles in podosomes
Supplementary Figure 3	Linescans showing resolution of 3B imaging in live cell samples.
Supplementary Figure 4	State transition diagram for our model of a fluorophore
Supplementary Note	Detailed description of 3B algorithm

Note: Supplementary Videos 1-7 and Supplementary Software are available on the Nature Methods website.

Nature Methods: doi:10.1038/nmeth.1812

Supplementary Figure 1 : The two graphs show a time-scan, each in a region with an isolate fluorophore, through a single pixel of the dataset used in Figure 2c–g. Single frame images of the corresponding fluorophore are shown next to each graph. Only the last 200 frames of the 500 frame dataset (which were usually discarded) were used in order to isolate individual fluorophores. The upper graph shows a dim, slowly blinking fluorophore with three appearances. The fluorophore is localised to a standard deviation of 31 nm using 19 frames (thresholded about 6200). The lower graph shows a bright fluorophore with two brief appearances. The fluorophore is localised to a standard deviation of 9.5 nm using 6 frames (thresholded above 6400).

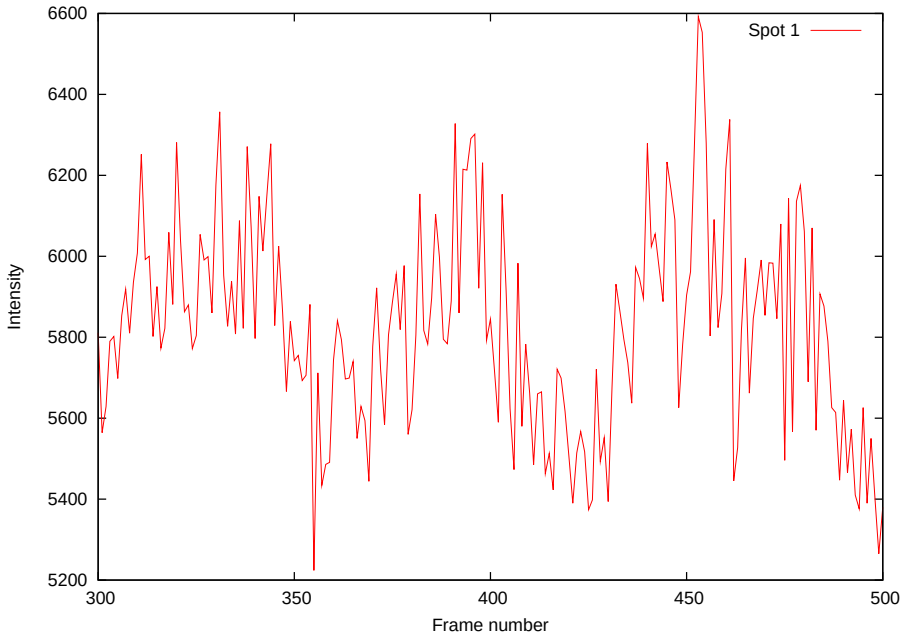

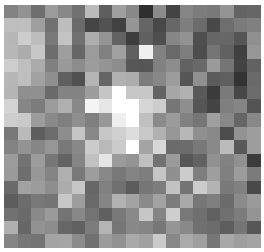

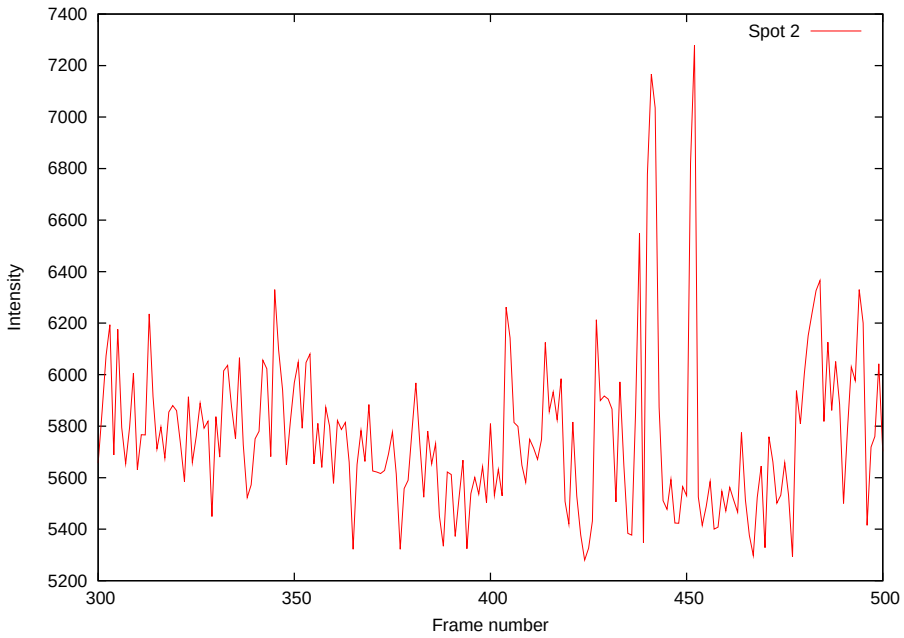

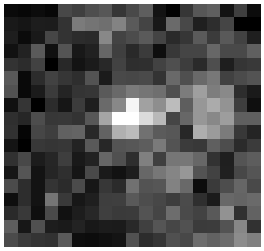

Nature Methods: doi:10.1038/nmeth.1812

Supplementary Figure 2 : We have compared the distribution of binding angles at junctions between vinculin strands in images obtained using our 3B analysis technique to the angles found using STED. The STED data has been taken from (M. Walde, J.M., G.E.J., R.H., S.C., Unpublished data), which also describes the method used to measure the angles. From the STED data, 1,780 angles were measured and from the localization data, 338 were measured. As can be seen, the results from the two microscopy techniques are in agreement, but the higher resolution of our technique produces a sharper peak in the angle distribution.

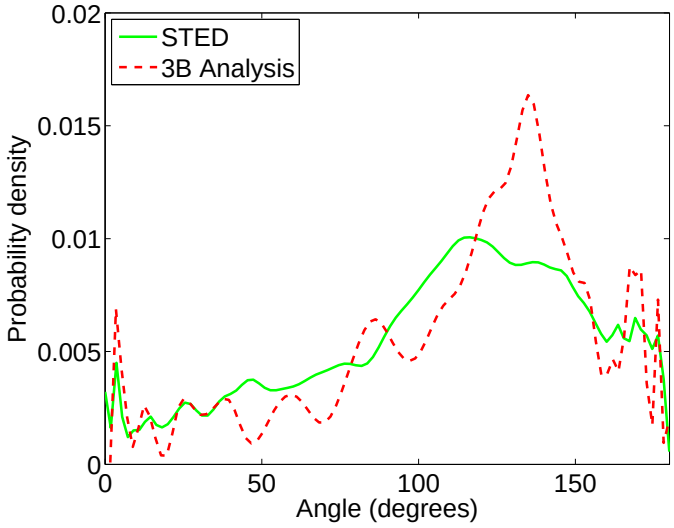

Supplementary Figure 3 : Linescans showing resolution of 3B imaging in live cell samples. (a), (b) two images of a podosome 20 seconds apart (see Figure 3a) with (c), (d) linescans. (e), (f) two podosomes (see Figure 4) with linescans (g), (h). Structures around 50nm apart can be seen in linescans (c), (g) and (h). Scalebars are 200 nm.

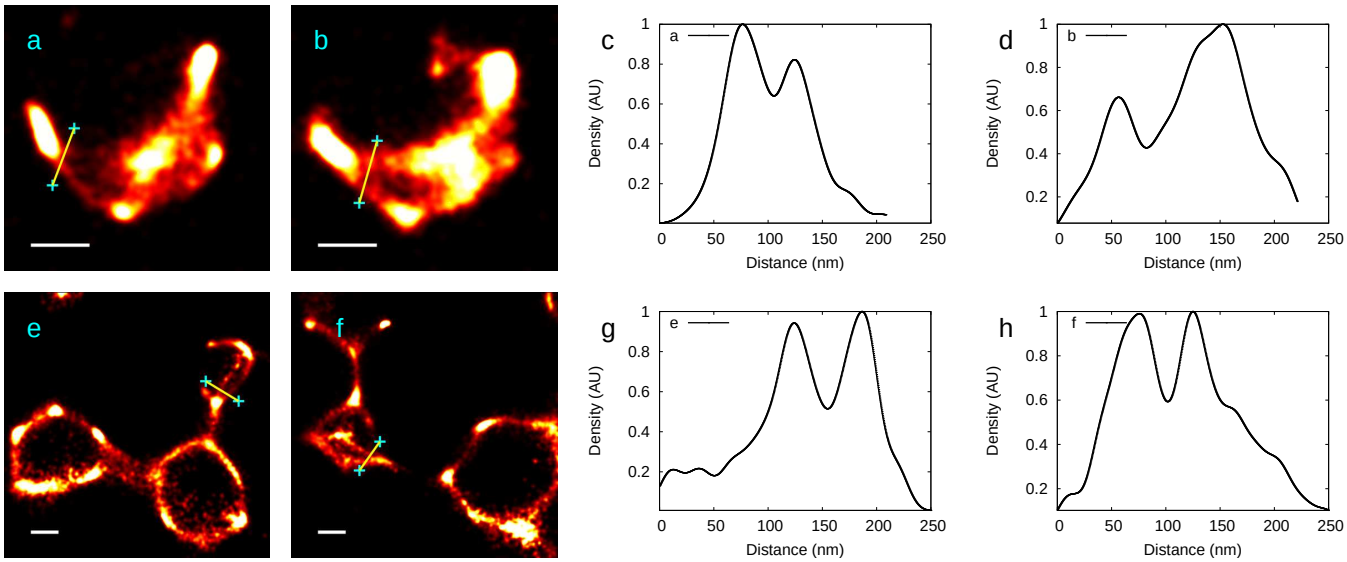

Nature Methods: doi:10.1038/nmeth.1812

Supplementary Figure 4 : State transition diagram for our model of a fluorophore.

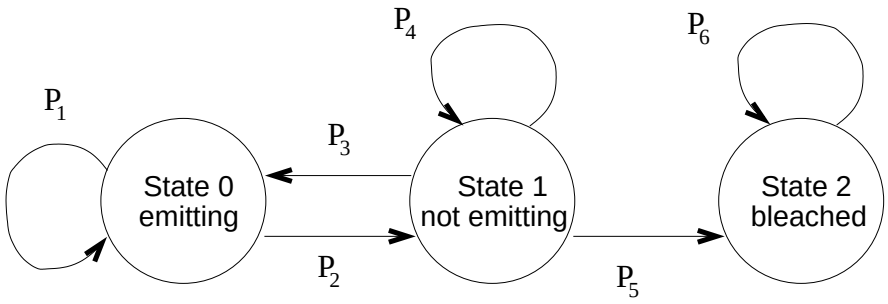

Supplementary Note 1 : Detailed description of method.

Modelling the image

Emitting fluorophores are modeled as producing a Gaussian shaped spot in the image. This spot has four continuous variables: the position (x,y), the radius, and the brightness (integrated intensity). We assume that fluorophores can occur anywhere in the region being analyzed with equal probability. Size and brightness are taken to be independent and prior distribution over the variables is set to log-normal, as this is a convenient distribution which prevents negative values. We normalize images by high-pass filtering with large Gaussian kernel to remove the background offset followed by scaling the image to set the standard deviation of intensity to one. This is possible because the images that we have analysed have very large areas containing only large amounts of out of focus light, which means that there are only small errors in the estimate of the noise variance. If the image is mostly foreground, then the noise variance can be estimated using manually selected background regions (which include the still present out-of-focus fluorescence). The prior on brightness is applied relative to the normalized image. Image noise is modeled as Gaussian with zero mean and the standard deviation (σ) of 1, since the background level is high.

Inference

Below, we use the convention common in the Bayesian machine learning literature that $P(\cdot)$ denotes both continuous and discrete probability distributions and the $\int$ symbol is used in both the discrete and continuous case. A complete list of symbols is given at the end of this note.

Consider the case of deciding to place a fluorophore, $\mathcal{F}$, versus keeping the null hypothesis that no fluorophore is present, $\mathcal{N}$, given the data, D. We would like to determine the relative probabilities $\frac{P(\mathcal{F}|D)}{P(\mathcal{N}|D)}$ and using Bayes' rule we obtain the Bayesian model comparison equation: $\frac{P(\mathcal{F}|D)}{P(\mathcal{N}|D)} = \frac{P(D|\mathcal{F})P(\mathcal{F})}{P(D|\mathcal{N})P(\mathcal{N})}$. Since $P(\mathcal{F})$ and $P(\mathcal{N})$ are constants, we need to calculate $P(D|\mathcal{F})$ and $P(D|\mathcal{N})$. The latter is trivial as it is just the probability of observing all pixels given the noise model. The former is computed by evaluating the model evidence which is computed using the marginalization:

$$P(D|\mathcal{F}) = \int_{a\in\mathbb{R}^4} \int_{b\in\mathbb{Z}_3^N} P(D,a,b|\mathcal{F})\,\mathrm{d}b\,\mathrm{d}a, \qquad (1)$$

where a are the four continuous parameters, b is the fluorophore state in each frame, and N is the number of frames. For a single fluorophore, the integration over b can be performed with the forward algorithm[24]. We perform the integral over the continuous parameters using using Laplace's Approximation[28] which involves finding a_{MP}, which is the MAP (maximum *a posteriori*) estimate of a. We also require the MAP probability, $P(D, a_{\mathrm{MP}}|\mathcal{F})$, and the Hessian, $\nabla\nabla \log P(D,a|\mathcal{F})|_{a_{\mathrm{MP}}}$, We find a_{MP} using nonlinear conjugate gradient[29].

We need to compare models with different numbers of fluorophores. For a model with M fluorophores, $\mathcal{F}_M$, a now has $4M$ continuous parameters: four per fluorophore. Also, $b = \{b_1, \cdots, b_M\}$, where $b_i \in \mathbb{Z}_3^N$ is the state sequence for the ith fluorophore. Equation 1 becomes

$$P(D|\mathcal{F}_M) = \textstyle\int_{a\in\mathbb{R}^{4M}} \int_{b\in\mathbb{Z}_3^{MN}} P(D,a,b|\mathcal{F}_M)\,\mathrm{d}b\,\mathrm{d}a,$$

Exact integration over state sequences rapidly becomes intractable with increasing M so we perform integration using MCMC (Markov Chain Monte Carlo) sampling. The discrete states are sampled using Gibbs sampling[30] since we can sample from Markov chains efficiently using forward filtering backwards sampling[31]. For convenience, we now make the definitions $P(D,a,b|\mathcal{F}_M) = P^*(a,b) = e^{E(a,b)}$, where E is the log probability. Also, we define $Z = P(D|\mathcal{F}_M) = \int\int P^*(a,b)\,\mathrm{d}a\,\mathrm{d}b$, $Z_a = \int P^*(a,b)\,\mathrm{d}b$ and $\frac{P^*(a,b)}{Z} = P(a,b)$.

We use Laplace's approximation to integrate over a. Recall that one requirement is computation of $Z_{a_{\mathrm{MP}}}$ which requires optimization over a to find a_{MP}. The latter is computed using the MCMC technique of slow growth thermodynamic integration[32,33] because while it is hard to compute $Z_{a_{\mathrm{MP}}}$ directly it is easier to compute the integral of the derivative of the log with respect to some parameter. The noise standard deviation, σ is the most convenient parameter so instead of keeping it fixed to 1, we treat it as a parameter and compute:

$$\log Z_a(1) = \log Z_a(\sigma_{\mathrm{MAX}}) - \int_1^{\sigma_{\mathrm{MAX}}} \frac{\mathrm{d}}{\mathrm{d}\sigma} \log Z_a(\sigma)\,\mathrm{d}\sigma. \quad (2)$$

For sufficiently large values of σ_{MAX} (e.g. 10^{10}), the HMM states become effectively independent of the data and so $\log Z_a(\sigma_{\mathrm{MAX}}) = -NK\log\sqrt{2\pi{\sigma_{\mathrm{MAX}}}^2}$, where K is the number of pixels.

As discussed before, finding a^* requires optimization over a to find the MAP fluorophore positions. For one fluorophore, we use conjugate gradient to optimize over a. However, since the sampling introduces noise in estimating Z_a, it it not possible to know if a true maximum or an artifact of noise has been found. Therefore we have developed a hybrid of the forward algorithm and MCMC to compute derivatives of Z_a very precisely. By yielding accurate estimates of the derivatives, we can avoid resampling during each loop of the optimization, which makes the process vastly more efficient and prevents the optimization from getting stuck on an artifact of noise.

Nature Methods: doi:10.1038/nmeth.1812

Since our method only yields accurate gradients, we adapt the conjugate gradient algorithm. While searching along the conjugate direction, instead of searching for a local maximum of Z_a, we search until the dot product of the first derivative and the search direction changes sign, and then identify the zero crossing. We take small steps to avoid jumping over the local maximum.

Our hybrid method works as follows. Derivatives of logarithms can be readily found using S samples drawn using MCMC[32] (where $\tilde{b}$ is an instance of a sample of b):

$$\frac{\mathrm{d}}{\mathrm{d}a}\log Z_a = \int \frac{\mathrm{d}E(a,b)}{\mathrm{d}a}P(a,b)\,\mathrm{d}b \approx \frac{P(a)}{S}\sum_{\tilde{b}\sim P(b|a)}\frac{\mathrm{d}E(a,\tilde{b})}{\mathrm{d}a}. \tag{3}$$

When finding the expectation of an arbitrary function ϕ over an arbitrary distribution $P(x)$ (with $x = \{x_1, \cdots, x_n\}$ in the arbitrary space $x \in \mathcal{X}, x_i \in \mathcal{X}_i$) using MCMC, the integration over different variables can be separated:

$$\int_{\mathcal{X}} \phi(x)P(x)\,\mathrm{d}x = \int_{\mathcal{X}_n\times\cdots\times\mathcal{X}_2}\left[\int_{\mathcal{X}_1}\phi(x)P(x_1|x_2\cdots,x_n)\,\mathrm{d}x_1\right]P(x_2,\cdots,x_n)\,\mathrm{d}(x_2,\cdots,x_n). \tag{4}$$

Since drawing samples from the joint draws samples from the marginal, this can be approximated easily using MCMC:

$$\approx \frac{1}{S}\sum_{(\tilde{x}_2,\cdots,\tilde{x}_n)\sim P(x_2,\cdots,x_n)}\left[\int_{\mathcal{X}_1}\phi(x_1,\tilde{x}_2,\cdots,\tilde{x}_n)P(x_1|\tilde{x}_2,\cdots,\tilde{x}_n)\,\mathrm{d}x_1\right]. \tag{5}$$

Substituting the derivative of $\log Z_a$ from Equation 3 into equation 5 gives:

$$\begin{aligned}\frac{\mathrm{d}}{\mathrm{d}a}\log Z_a &= \int_{\mathbb{Z}_3^{MN}}\frac{\mathrm{d}E(a,b)}{\mathrm{d}a}P(a,b)\,\mathrm{d}b \\ &\approx \frac{P(a)}{S}\sum_{(\tilde{b}_2,\cdots,\tilde{b}_M)\sim P(b_2,\cdots,b_M|a)}\left[\int_{\mathbb{Z}_3^N}\frac{\mathrm{d}E(b_1,\tilde{b}_2,\cdots,\tilde{b}_M,a)}{\mathrm{d}a}P(b_1|\tilde{b}_2,\cdots,\tilde{b}_M,a)\,\mathrm{d}b_1\right].\end{aligned} \tag{6}$$

In a manner similar to Equation 3, the inner integral in Equation 6 can be written as:

$$\frac{\mathrm{d}}{\mathrm{d}a}\log\int_{b\in\mathbb{Z}_3^N}P^*(b_1|\tilde{b}_2,\cdots,\tilde{b}_M,a)\,\mathrm{d}b_1. \tag{7}$$

This equation is the marginalization equation for a single fluorophore, conditioned on a sample of all other fluorophore states and it can therefore be efficiently computed with the forward algorithm. We can therefore compute gradients with respect to the parameters of a spot by marginalizing over the spot's states with the forward algorithm and the remaining spot states with MCMC.

Using this hybrid of MCMC and the forward algorithm, we get smooth, accurate differentials because we do not recompute the samples during the hill climbing stage. This allows for very efficient optimization of the real-valued fluorophore parameters and is crucial to the success of our method.

Algorithm

Even with these improvements, it is too computationally expensive to compare large models with Bayesian model comparison. In practice, we make many local decisions which incrementally modify the model, one fluorophore at a time. We take one fluorophore under consideration to be either added or removed. We either select a fluorophore for removal, or add a new fluorophore at a random position. We now have two models: one with that fluorophore and one without. For the purposes of model selection and marginalization, we allow only the parameters of that one spot to vary, and then decide which model to keep. After a number of such decisions have been made, we re-optimize the entire model, then repeat the model selection process. This yields the algorithm:

Nature Methods: doi:10.1038/nmeth.1812

1. Select initial spot positions for a model.
2. Optimize model using hybrid MCMC and adapted conjugate gradient. The step size is limited so that L_∞ of the step is 0.5. One pass of optimization optimizes each fluorophore in turn with the ordering of fluorophores taken in the four compass directions. We repeat this for 4 passes (one for each compass direction), using 10 samples.
3. Repeat 20 times:
   (a) Compute free energy (Z_a) of the model assuming fluorophores are fixed using 1000 iterations of thermodynamic iterations where the noise standard deviation for iteration i is $1.25^{i/10}$.
   (b) Either add a new fluorophore or select one at random.
   (c) Optimize the new/selected spot using the hybrid method with 20 samples.
   (d) Compute Z_a of the new model using thermodynamic integration.
   (e) Compute free energy by computing the Hessian using 100 outer samples, and 1000 inner samples.
4. Goto 2

Note that when computing the Hessian with respect to the parameters of a single spot, we do not have an equivalent to the hybrid algorithm, so we use a nested iteration scheme. During the nested scheme, for each sample of all states we draw (*outer sample*), we draw a number of samples (*inner samples*) from the Markov chain of interest using forward filtering, backwards sampling. Since that algorithm is so efficient, this allows us to get considerably more accuracy with little extra computational cost.

Note that in general, estimating a suitable point for terminating an MCMC procedure is difficult[32]. In practice, the algorithm is run until significant changes in the reconstructed image can no longer be observed. This typically requires several hundred complete iterations.

Reconstruction

The method for generating a final image from the MAP estimates is very similar to a discrete approximation to kernel density estimation. The first stage is to build up an image containing the fluorophore density. An empty image is initially created which is generally a much higher resolution than the input data.

All MAP positions are then quantized to the nearest pixel in the high resolution density image. The resulting quantized locations are then accumulated into the image. In order to retain an approximation of the brightness, the accumulated fluorophores are weighted with the MAP brightness.

The resulting high resolution image is then blurred with a Gaussian kernel with a standard deviation of not less than $\sigma = 2$ pixels, then subsampled by a factor of two to give the density image. The density image is then given a false colormap, to create the final colormapped image. The density image intensity is then scaled by an arbitrary amount and a glow color scheme is then applied using the following formula:

$$\begin{aligned} r &= \min 1, 3d \\ g &= \min 1, (\max 0, 3d - 1) \\ b &= \min 1, (\max 0, 3d - 2)\,, \end{aligned}$$

where d is a pixel intensity in the scaled density image, and r, g and b are the corresponding reg, green and blue pixel intensities in the final colormapped image. All the 3B images shown in the paper are generated using this method, except for Figure 2a, which shows a single MCMC sample.

Additional references

29. Press, W. H., Teukolsky, S. A., Vetterling, W. H., and Flannery, B. P. *Numerical Recipes in C.* Cambridge University Press, (1999).
30. Geman, S. and Geman, D. Stochastic relaxation, Gibbs distributions, and the Bayesian restoration of images. *IEEE T. Pattern Anal.* **6**(6), 721–741 (1984).
31. Godsill, S. J., Doucet, A., and West, M. Monte carlo smoothing for nonlinear time series. *J. Am. Stat. Assoc.* **99**(465), 156–168 March (2004).
32. Neal, R. M. Probabilistic inference using markov chain monte carlo methods. Technical Report CRG-TR-93-1, Dept. of Computer Science, University of Toronto, (1993).
33. Bash, P., Singh, U., Langridge, R., and Kollman, P. A. Free energy calculations by computer simulation. *Science* **22**, 245–268 (1987).

Table of symbols

Symbol	Meaning
N	Number of frames in an image sequence.
M	Number of fluorophores.
S	Number of samples.
$\mathbb{Z}_3$	Integers modulo 3, i.e. $\mathbb{Z}_3 \equiv \{0, 1, 2\}$. This is generally used to indicate that a variable is in one of the three states, emitting (light), not emitting and bleached.
$\mathbb{Z}_3^N$	An N dimensional quantity, each element of which is in $\mathbb{Z}_3$. A variable in $\mathbb{Z}_3^N$ is generally the states of a single fluorophore in all frames.
$\mathbb{Z}_3^{MN}$	An MN dimensional quantity in $\mathbb{Z}_3$. A variable in this space contains the state of every fluorophore in every frame.
b	A variable containing the state of every fluorophore in every frame.
$\mathbb{R}^4$	Real numbers in 4 dimensions.
a	A variable containing the four continuous parameters of every fluorophore: x and y position, brightness and size.
$\mathcal{N}$	Model class for the null hypothesis (data is generated by noise).
$\mathcal{F}$	Model class indicating that the data is generated by one fluorophore and noise.
$\mathcal{F}_M$	Model class indicating that the data is generated by M fluorophores and noise.
σ	Noise standard deviation, usually set to 1.
$P(D, a, b\|\mathcal{F}_M)$	Probability that the data is generated by a M fluorophores with specific parameters and a specific state sequence, multiplied by priors over b and a.
$P^*(a, b)$	Shorthand for above.
$P(D\|\mathcal{F}_M)$	Probability that data is generated by M fluorophores. Equal to $\int\int P^*(a, b)\,\mathrm{d}a\,\mathrm{d}b$
Z	Shorthand for above. Note that $\int\int P^*(a, b)/Z\,\mathrm{d}a\,\mathrm{d}b = 1$.
$P(a, b)$	Normalized distribution $P^*(a, b)/Z$.
$\tilde{b}$	A sample of b drawn from the distribution $P(b\|a)$.
$P(a)$	Prior probability of a. Equivalent to $P(a\|\mathcal{F}_M)$.
$E(a, b)$	Log probability such that $P^*(a, b) = e^{E(a,b)}$.
$P(b^0)$	Prior probability of the fluorophore state in the first frame. Equivalent to $P(b\|\mathcal{F}_M)$. This is set to give a 50/50 chance of being in states 0 or 1.
a^0	Initial spot parameters.
$P(D, a\|\mathcal{F}_M)$	Probability that the data is generated by a M fluorophores with specific parameters, but with the state sequence marginalized out.
Z_a	Shorthand for above.
$Z_a(\cdot)$	Z_a parameterized with the noise standard deviation. Since σ is usually 1, the parameterization is usually omitted.
a_{MP}	The value of a which maximizes Z_a.
$\mathcal{X}$	An arbitrary space.
x	An arbitrary variable in $\mathcal{X}$.
ϕ	An arbitrary function of x.
$P_1 \cdots P_6$	Transition matrix probabilities.

Parameter values and adjustments:

$P_1 \cdots P_6$	Discussed in the main text.
$P(a)$	All elements of $P(a)$ are independent. The position prior is set to be uniform over the area under analysis and zero outside. The size prior is set to be a log-normal distribution with $\sigma = 0.1$ and μ set so that the mode is at the correct FWHM of the PSF for the microscope. The brightness prior is log-normal with values around $\sigma = 3$ $\mu = 1$. These parameters need to be tuned to the data based on the approximate brightness of the fluorophores.
a^0	The initial values of the brightness and size are set to the modal values of the prior. The initial number of spots needs to be selected by the user. The initial positions are approximately uniform over the area of interest.

The parts of $P(a)$ which relate to the pixel resolution and relative brightness may need to be adjusted for different samples. The part of $P(a)$ and a^0 relating to the area of analysis will need to be altered between different runs of the algorithm.